X-ray Visible Collagen Scaffolds by Bulk Iodination

Carlos Flechas-Becerra[1], Lady Barrios-Silva[2], Ebtehal Ahmed[1], Joseph C. Bear[3], Zhiping Feng[1], David Y.S. Chau[2], Samuel G. Parker[4], Steve Halligan[4], Mark F. Lythgoe[1], Daniel J. Stuckey[1], P. Stephen Patrick[1*]

1. Centre for Advanced Biomedical Imaging, Division of Medicine, University College London, London, WC1E 6DD, UK

2. Division of Biomaterials and Tissue Engineering, Eastman Dental Institute, University College London, Royal Free Hospital, Rowland Hill Street, NW32PF, London, UK

3. School of Life Science, Pharmacy & Chemistry, Kingston University, Penrhyn Road, Kingston upon Thames, KT1 2EE, UK

4. Centre for Medical Imaging, University College London UCL, Charles Bell House, 43-45 Foley Street, London, W1W 7TS, UK

*Corresponding author: peter.patrick@ucl.ac.uk

Abstract (250) @250

We present a fast, simple, and novel solution to the problem of non-invasively imaging transplanted protein-based scaffolds – facilitating high-resolution, long-term tracking with X-ray CT. This was achieved via bulk iodination of tyrosine residues under mild conditions (pH 7.4) using potassium tri-iodide and phosphate buffered saline. This addresses the problem of visualising implanted protein-based biomaterials, which are difficult to locate with typical non-invasive imaging approaches due to similarities with endogenous tissue. This method promises to address previously unanswered questions on their correct delivery to the target site, degradation rate, migration, and structural integrity – accelerating optimisation and safe translation of new collagen-based therapies.

To illustrate the utility of this approach, we label a clinically approved, commercially available collagen-based hernia repair mesh (based on decellularised porcine dermis), and show maintained morphological and mechanical properties post-labelling. In a mouse model of hernia implantation, the labelled hernia mesh retained significant X-ray visibility above unlabelled control material and muscle at all time points up to 3 months post-implantation, together with an unchanged degradation rate and inflammatory response. Supporting translation of this technology, contrast was stable over 15 months in saline at room temperature, and X-ray exposures below those typically used in the clinic still showed good contrast of the labelled scaffolds versus surrounding tissues *in vivo.*

We further show that this labelling technique is compatible with a range of therapeutically relevant formats including bovine, porcine and jellyfish collagen, as well as silk sutures, illustrating this technique's utility across a range of surgical and regenerative medicine applications.

Introduction

The use of extra-cellular matrix (ECM) materials is widespread in regenerative medicine (1), with collagen-based products clinically established for the repair of urogenital damage, skin wounds, bone defects, hernia, post-surgical reconstruction, and cardio-vascular disease (2-7). As the main structural protein in the ECM, collagen makes up around a third of the total polypeptide mass of the human body (8). Here it provides tuneable mechanical and biochemical properties through its numerous pre and post-translational modifications, ligand attachment sites (9), tissue-specific proteoforms, and supramolecular assemblies (10).

Close matching of collagen-based materials to the needs of a given therapy, target tissue or implantation site can thus be achieved either through the endogenous variety and complexity of various decellularised donor tissues (dermis, aortic valves (11), lung (12), heart (13, 14) *etc.*), or by synthetic bottom-up engineering to allow complete design of the material (15, 16). A range of manufacturing technologies including 3D printing, electrospinning, moulding, microfluidic encapsulation, acoustic cell-patterning, crosslinking, and composite and modular assembly also allow artificial control of its degradation rate, structure, and patterning across multiple length scales (3, 17-20). Multiple sources contribute to the good availability of collagen, with porcine, bovine, marine, and recombinant proteins remaining suitable for human use due to their low immunogenicity (4, 15).

Despite being one of the most well-established biomaterials, research into collagen for tissue engineering applications has continued to grow over three-fold in the last 20 years (15) - in part due to its versatile role as a scaffold for emerging technologies. In this way, unmet needs in spinal cord damage (21), cartilage and connective tissue defects, tooth (22) and heart regeneration (19) are being approached through its combination with stem cells, differentiated cells, growth factors, nanoparticles, and advanced patterning and fabrication technologies. However, for these and other novel approaches to become mature clinical products, their behaviour and safety post-implantation will need to be validated– a challenge that is difficult to meet without the use of non-invasive imaging (23, 24). However, the physical similarity between collagen-based implants and native tissue often makes this challenging, with each producing comparable signal on most medical imaging modalities including MRI, CT, and ultrasound. This leaves details of successful delivery and integration, mis-delivery, mechanical failure, or detachment difficult to monitor in either preclinical models, or patient populations.

To address this, we demonstrate a fast and simple labelling approach for producing radiopaque, X-ray visible collagen. Here we took inspiration from the radiochemistry literature, adapting two existing iodination reactions previously used to attach radioactive iodine isotopes (^{123}I, [124]I, or ^{131}I) to tyrosine residues in soluble proteins such as antibodies (25). To our knowledge, this is the first time either of these reactions have been applied for the purpose of producing X-ray CT-based contrast, or adapted for use on macromolecular protein scaffolds with or without use of a stable iodine isotope.

Firstly, we tested a modified version of the potassium tri-iodide reaction (26), popularised by Pressman and colleagues in the late 1940s (27-29). To adapt this for non-radio-labelling purposes, we used a preparation of Lugol's iodine as a source of potassium tri-iodide (KI_3), keeping the original optimised pH of the reaction at 7.4. Secondly, we evaluated McFarlane's method of the 1950s, which uses iodine monochloride (ICl) at a pH 8.5. Both produce mono (3-iodo-tyrosine) and di-iodo tyrosine (3,5-iodo-tyrosine), in varying ratios depending on reaction time and iodine concentration, with the higher pH of McFarlane's reaction also contributing toward the iodination of histidines (30). Tyrosine was deemed to be a suitable target for iodination in collagen due to its low but consistent

molar fraction (0.3 and 2%) of the amino acid residues across the tissues of various mammalian and aquatic species (31, 32). Unlike proline and glycine which are arranged periodically along the whole length of collagen, tyrosine is concentrated at the end of chain, and not known to be involved in the hydrogen bonding interactions that determine collagen's triple-helical structure - making it a good labelling target with low potential for disrupting stability and function (8). To demonstrate the retention of relevant material and biological properties post-labelling we present the results of mechanical testing, scanning electron microscopy (SEM), Energy Dispersive X-ray spectroscopy (EDS) and *ex vivo* histological analysis.

To illustrate the utility of this labelling method, we apply it here to improve the radiological visibility of hernia meshes, which is currently poor and is known to affect their clinical management (33). Labelling of meshes with a radiopaque marker has previously been suggested as a solution to this (34), providing an obvious illustration of this method's utility. With mesh-based hernia repair being the most performed surgical technique worldwide at around 20 million operations per year globally (and with a ~10% complication rate), this provides existing demand for implementation of this imaging strategy (35). To this end, we demonstrate tracking of an iodinated collagen-based hernia mesh *in vivo* up to three months post implantation, with comparable biological response of the labelled mesh versus an unmodified off-the-shelf control established via histology.

In summary, this method presents a fast, simple, and cheap route of labelling pre-formed collagen-based biomaterials for detection with one of the most widely-available clinical imaging modalities - X-ray CT. We show that this labelling method is achievable under mild and scalable conditions, maintaining the biocompatibility and strength of the starting material. To demonstrate the utility of this method, we label a clinically approved, commercially available collagen-based hernia mesh, and quantify its improved contrast in a mouse model up to three months post implantation using non-invasive CT imaging. For future application, we also demonstrate that this labelling method enables X-ray CT detection of a range of other protein-based materials used surgically and in tissue engineering, including silk sutures and egg shell membrane.

Results

Potassium Triiodide and Iodine Monochloride methods enhance radiopacity of collagen scaffolds

The efficacy of both candidate iodination reactions (Potassium Triiodide - KI_3, and Iodine Monochloride - ICl) was evaluated on samples of a representative clinically approved collagen scaffold produced from decellularised porcine dermis (XenMatrix™ hernia mesh, Bard). Two buffers were compared per reaction, chosen for their suitable pH range and established use in protein biochemistry – Phosphate buffered saline (PBS) and HEPES for the KI_3 method (at pH 7.4), and Glycine and Tris buffers for the ICl method (at pH 8.5) (36), see figure 1A. Each reaction/buffer combination increased the radiopacity of the labelled materials, with significant increases in HU being measured with X-ray CT versus unlabelled control samples (Fig 1B). For the KI_3 method, PBS showed superior labelling to HEPES buffer, consistent with its previously-reported acceleration of tyrosine iodination (37).

Assuming a radiopacity of iodine of 14-16 HU per mg Iodine / mL (38), a tyrosine weight fraction of 1.96% for porcine collagen type 1 (UniProt ref: A0A287BLD2), and a protein weight / volume fraction for decellularised porcine dermis of 40% (39), then total di-iodination of tyrosine residues would give an expected increase in radiopacity of 154-175 HU. This was comparable to the

increase in HU measured for KI_3 with HEPES buffer (112 HU) and PBS (160 HU), see figure 1B. Fluorescence spectroscopy gave a characteristic 300 nm peak for tyrosine in control (unmodified) samples, which decreased significantly in intensity by 98% following labelling with either KI_3/PBS or ICl/Glycine reactions (Figure S1, n=3, p<0.005 2-tailed t-test). This is consistent with previously reported decreases at the 300nm tyrosine fluorescence peak following iodination of tyrosine residues (40, 41), and complete conversion of tyrosine to di-iodotyrosine in soluble collagen under similar conditions (42).

Interestingly the iodine monochloride reaction showed significantly higher levels of CT contrast (p<0.05 versus KI_3/PBS, students 2-tailed *t*-test; 210 HU for Glycine buffer, 226 HU for Tris buffer), suggesting additional sites of modification. This is consistent with previous reports of histidine iodination occurring in addition to tyrosine iodination above pH 8 (30, 43), with mono-iodination of histidine in addition to di-iodination of tyrosine giving a predicted increase of 220-251 HU.

Homogeneity of labelling, and iodine incorporation throughout the scaffold, was confirmed by plotting line profiles of signal intensity for samples labelled with each of the four reaction combinations (Fig 1C). To assess the stability of labelling, samples were incubated at 37°C in human serum for 16 days, with measurements of radiopacity taken at intervals using X-ray CT (Fig 1D). No decrease in contrast was measured over this period, suggesting stable iodine retention within the material under biologically-relevant conditions.

To ensure greater selectivity of modification and minimise alterations to the biological function of collagen, the milder conditions of the potassium tri-iodide method were chosen for use throughout the rest of this study, unless otherwise indicated. Potassium triiodide, in the form of Lugol's Iodine as used here, also has the advantage of being clinically established in its own right as an antiseptic, further increasing the feasibility of translating its use here for tracking labelled materials in patients.

To demonstrate the versatility of this labelling method we next labelled four additional protein-based materials of interest (Fig. 1F-J). NeuraGen (Fig. 1G) is an FDA-approved hollow tube formed of porous bovine collagen, implanted for the repair of peripheral nerve damage (44), and now being studied in combination with autologous stem cell therapy (45). However, its implantation has been reported to be surgically challenging, requiring the location and removal of implants when unsuccessful (46). Labelling with KI_3/PBS gave an increase in radiopacity of ~200 HU (Fig. 1G), and stability of labelling was confirmed up to 15 months at room temperature in saline (Fig. S2). We also labelled egg-shell membrane (ESM) (Fig. 1H), which contains a number of proteins alongside type I and type IV collagen (47). ESM is typically discarded as a waste product from the food industry, but due to its favourable biocompatibility and material properties is attracting attention as a new scaffold for tissue engineering and cell therapy (48-50). Again, an increase of ~200 HU was achieved with KI_3/PBS (Fig 1H), and stability of labelling was preserved over 15 months post-labelling, with no significant decrease over this period (Figure S3). We next demonstrated that a commercially-available hydrogel of "Type 0" Jellyfish-derived collagen could also be labelled and imaged (Fig 1I), which has been suggested as a more sustainable alternative to the established porcine and bovine collagen typically used in clinical applications (51, 52). Finally, we labelled a commercially-available silk-suture (Ethicon, 3-0), which showed an increase in HU of over ~1200 (Fig. 1J), consistent with the unusually high tyrosine content of silk worm silk (*Bombyx mori*), at 5 to 6-fold that of collagen (UniProt: P05790 · FIBH_BOMMO).
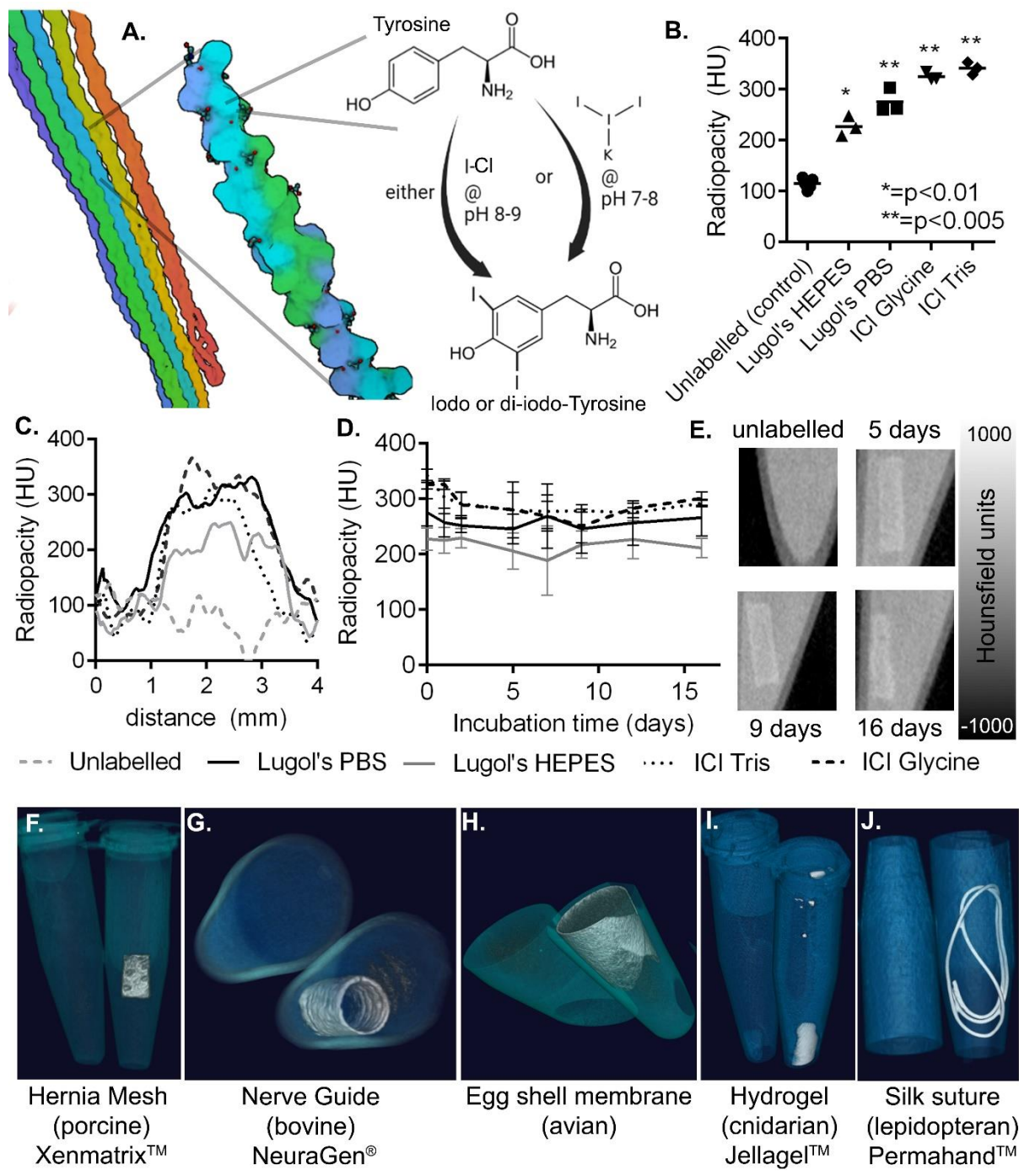
Figure 1. A. Schematic of collagen labelling showing colour-coded collagen fibrils and chains respectively, with iodination of a tyrosine residue following reaction with KI_3 or ICl. **B.** Increased radiopacity of porcine collagen scaffolds (Xenmatrix[TM]) vs unlabelled controls, following Potassium Tri-iodide (Lugol's) reaction or Iodine monochloride reaction (ICl) in the indicated buffers (unpaired, 2-tail *t*-test). **C.** Cross-sample intensity profile shows relative homogeneity of sampling for each of the reaction conditions. **D.** Increased radiopacity was retained up to 16 days of incubation at 37°C in human serum. **E.** Representative X-ray CT sections showing unlabelled and labelled (potassium tri-iodide reaction in PBS) hernia mesh sample following incubation in human serum. **F-J**. 3D rendered X-ray CT images of unlabelled (left tube) and labelled (right tube, potassium tri-iodide reaction in PBS) Hernia mesh, nerve guide, egg shell matrix, jellyfish collagen hydrogel, and silk suture.
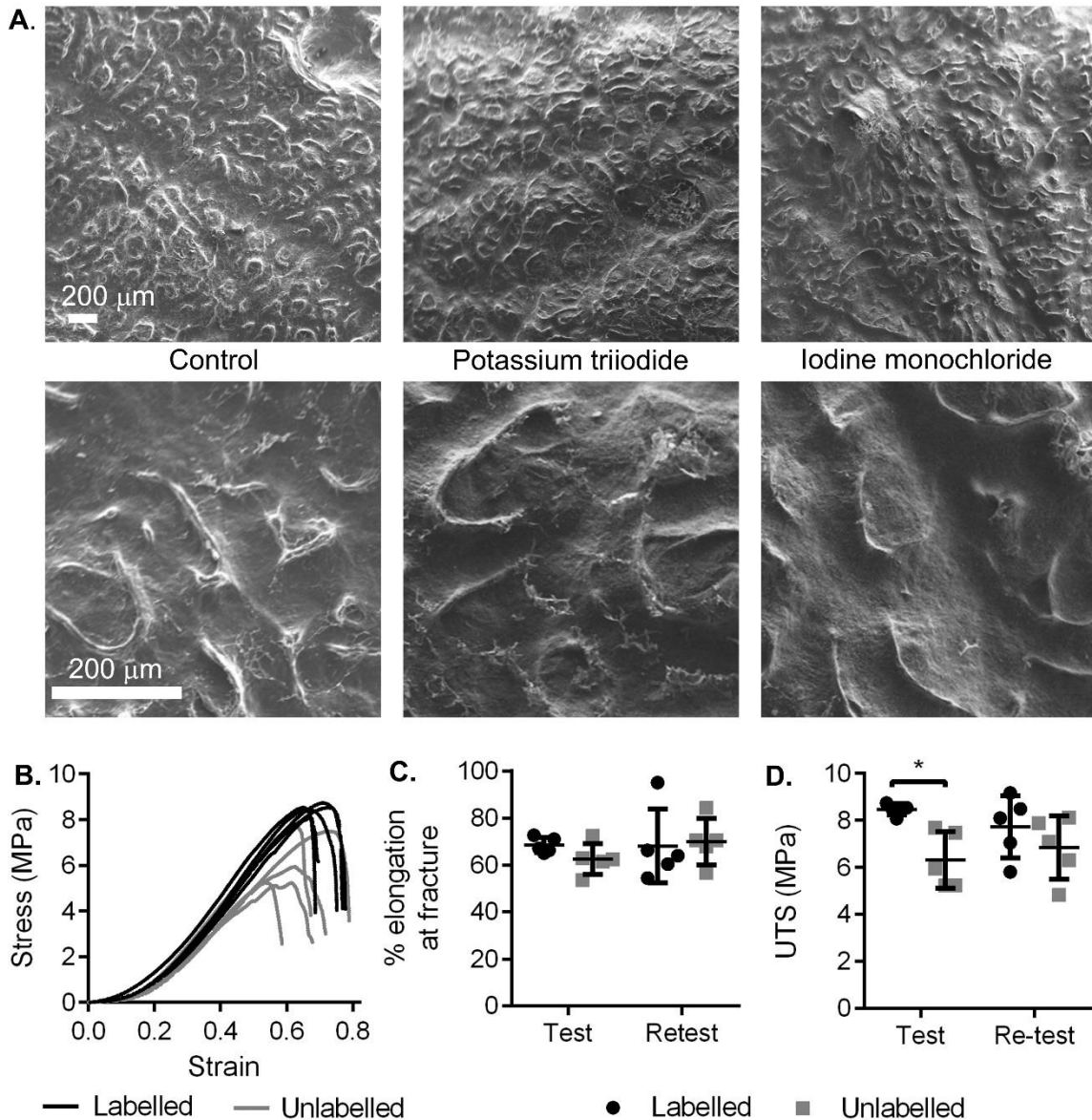
Figure 2. A. Surface morphology is comparable between control (unlabelled) collagen scaffolds and those labelled using Potassium triiodide and Iodine monochloride methods, as seen with scanning electron micrographs at two levels of magnification. **B.** Stress strain curves of labelled and unlabelled meshes, one line per replicate. **C.** No significant difference was found between labelled and unlabelled scaffolds in elongation percentage at point of fracture (2-tailed t-test). **D.** Labelled meshes required a significantly higher max force to induce fracture in primary tests, but not retests (p<0.05, 2-tailed t-test), indicating increased strength. N=5, lines show the mean, error bars show the standard deviation.

Surface morphology and material strength are preserved post-iodination.

To establish the preservation of native surface structure, collagen scaffolds (Xenmatrix™ hernia mesh) labelled with potassium tri-iodide (PBS buffer), and iodine monochloride (glycine buffer) were analysed using SEM and compared to unmodified samples. No change in large- or small-scale

structure could be seen after labelling with either reaction (Fig 2A), consistent with the mild reaction conditions. EDS analysis confirmed the presence of iodine only in the labelled samples (Fig. S4-7).

Dynamic mechanical analysis testing of control and potassium tri-iodide (PBS) labelled collagen scaffolds (Xenmatrix^{TM} hernia mesh) showed broadly comparable stress-strain curves (Fig 2B), and percent elongation at fracture (Fig 2C). The ultimate tensile strength (UTS) was however significantly increased in labelled vs unlabelled meshes (Fig 2D; 8.46 ± 0.24 (SD) MPa vs 6.32 ± 1.19 MPa, p<0.005 2-tailed t-test), though within the range of 2.53 ± 0.25 MPa to 28.54 ± 1.99 MPa reported for bovine and porcine-derived biological hernia meshes in the literature (53). This difference was not significant upon re-testing the material (7.72 ± 1.31 vs 6.84 ± 1.33, p=0.32), suggesting that the effect of iodination on material behaviour was at least partially reversible with stretching. Similarly, a small but significant increase in Young's modulus was measured upon labelling from 15.3 to 18.1 (p<0.01, student's 2-tailed t-test), which again was reversible post-stretching. FT-IR and Differential Scanning Calorimetry showed comparable spectra for labelled and unlabelled materials, albeit with minor peak shifts presumably due to the incorporation of iodine (Fig S8,9).

Iodinated hernia meshes remain trackable up to 3 months *in vivo*

To demonstrate the utility of this labelling approach for a clinically-relevant scenario, we subcutaneously implanted immunocompetent mice with labelled (KI$_3$/PBS) and unlabelled samples of the collagen-based hernia mesh (Xenmatrix^{TM}). X-ray CT imaging at intervals from the day of implantation to 3 months (12 weeks) post-implantation showed significant differences in radiopacity (HU) between labelled and unlabelled meshes (p<0.0001 at all time points, unpaired 2-tailed t-test), and between labelled meshes and muscle within the same animal (p<0.0001 at all time points, paired 2-tailed T-test), confirming the retention of radiopacity over time (Fig 3A-C). No difference in radiopacity between unlabelled meshes and muscle was found (p>0.05, paired 2-tailed t-test), consistent with the existing challenge in identifying commercially-available meshes from surrounding tissue. Illustrating the utility of this approach in detecting migration of materials from the site of implantation, one labelled mesh was found to move laterally between the day of implantation and the subsequent imaging time point of 1 week post-implantation (Fig 3D) – a phenomenon which occurs clinically following the failure of surgical attachment of meshes to the surrounding tissue.

Mesh visibility is preserved with reduced scan time and clinically-relevant X-ray doses

To assess the feasibility of imaging the labelled material under clinically-relevant x-ray doses, we imaged the implanted meshes with a range of scan times at 2 and 3 months post-implantation. At all scan times between 4 minutes and 4 seconds, labelled meshes showed good visibility on CT sections (Fig 4A) and a significantly higher HU than both muscle and unlabelled meshes following region of interest analysis (Fig 4B). To put these results into perspective, average clinical volumetric CT doses of 25 and 17 mGy (with 1 mGy equalling 1 Joule of energy absorbed per kg) were reported for abdominal imaging in Europe and the US respectively (54), which corresponded most closely to our 18 second / 16.4 mGy scan. This X-ray dose was sufficient to produce comparable quantification of intensity (HU) to the 4-minute scan for mesh and muscle, and to visualise the migrated mesh at 3 months post-implantation in 3D following intensity-based 3D rendering (Fig 4D).
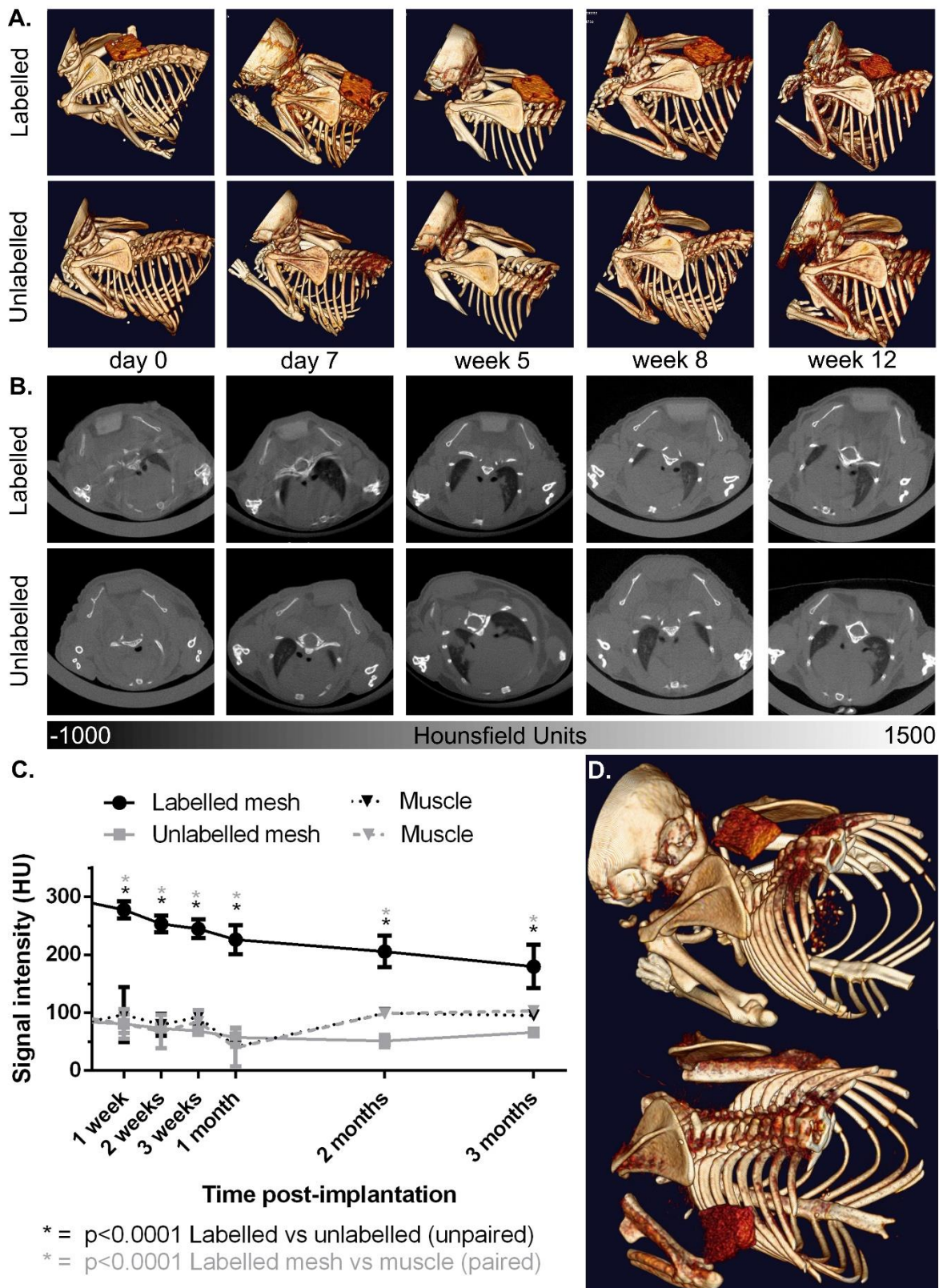
Figure 3 Iodinated hernia mesh samples (Xenmatrix) show increased visibility on X-ray CT vs unlabelled samples and muscle over 3 months post implantation on **A.** 3D reconstructions, **B.** axial CT cross sections, and **C.** region of interest quantification of x-ray absorbance (HU). Holm-Šídák multiple comparison tests show significantly higher radioapacity of labelled meshes vs muscle (paired), and vs unlabelled samples (unpaired) at all time points. N≥3 per time point, error bars show

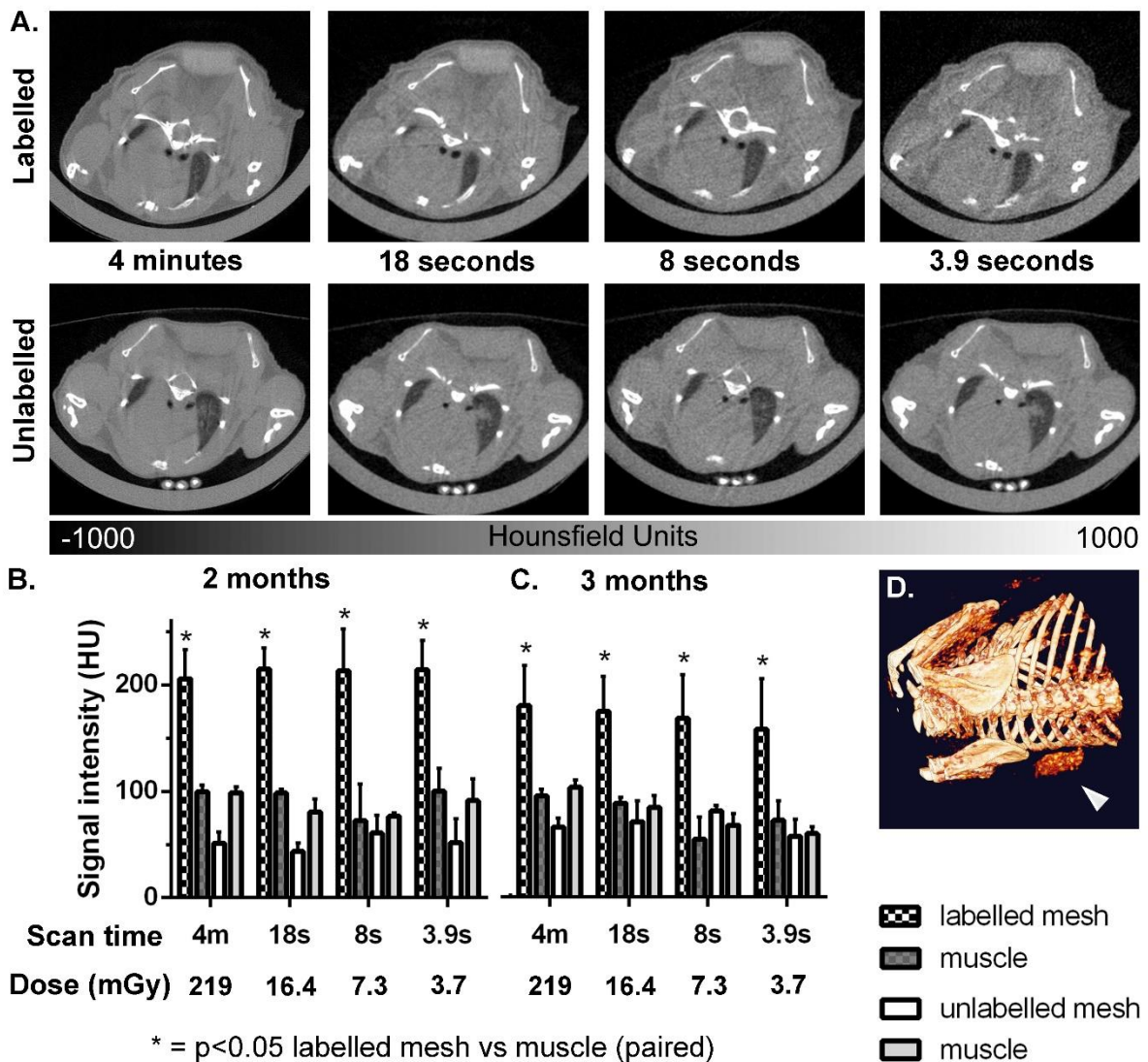standard deviation. **D.** CT renderings showed lateral mesh migration in one animal post implantation.

Figure. 4. Labelled meshes retained their increased visibility vs muscle and control mesh with decreasing scan times, as shown here with **A.** axial CT sections at 3 months post-implantation, and region of interest quantification of radiopacity at **B.** 2 months, and **C.** 3 months post-implantation, with Holm-Šídák multiple comparison tests. N≥3 per time point, error bars show SD. **D.** Laterally migrated mesh visualised on a 3D rendered 18 second CT scan at 3 months post-implantation using a clinically relevant X-ray dose of 16.4 mGy.

Labelled meshes show comparable immune response to unlabelled meshes *in vivo*

To assess the effect of iodination on the immune response to implanted meshes, samples were explanted at 2, 4, and 12 weeks post implantation, and H and E staining was performed on histological sections (Fig 5 A). Neutrophil and lymphocyte numbers were counted at 40× magnification by a trained histopathologist on n≥5 sections per time-point and sample (Fig. 5B), showing comparable numbers between labelled and unlabelled meshes at each time point (p>0.05 2-tailed unpaired T-tests). Infiltration of native tissue into the meshes was comparable in labelled

and unlabelled meshes, with representative sections at at 12 weeks post-implantation shown in Fig C,D.

Degradation rates comparable for labelled and unlabelled meshes
To further investigate the biological response to labelled meshes, samples were explanted at 2, 4, and 12 weeks, and stained using Picro Sirius Red stain for collagen (Fig 5 E,F). Labelled and unlabelled meshes appeared similar at each time point, with quantification of stained area showing no significant difference in coverage between mesh types at any time point. A trend decrease in coverage was seen over time for both meshes. No change in overall mesh volume for labelled meshes was measured based on semi-automatic intensity-based segmentation of the labelled implants (Fig S10), consistent with the overall preservation of collagen coverage seen histologically.
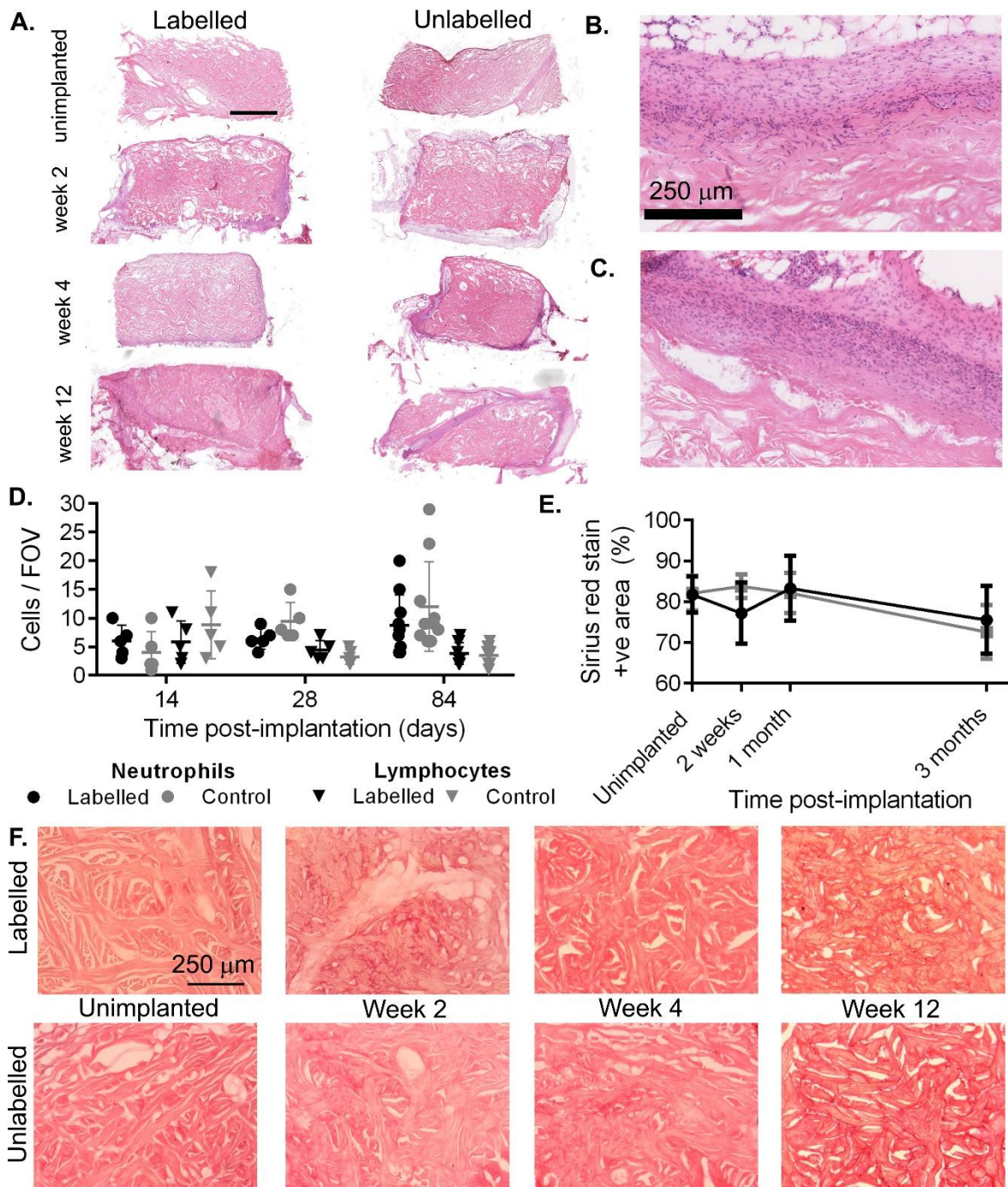
Figure 5. A. Macroscopic H and E stained sections of explanted meshes at 2, 4, and 12 weeks post-implantation. Scale bar = 1mm. Representative sections showing comparable infiltration of endogenous tissue at the mesh boundary at 12 weeks for **B.** labelled, and **C.** unlabelled meshes. **D.** . No significant difference was found between mean neutrophils and lymphocytes counts at 40x magnification in H and E stained tissue sections at 2, 4, and 12 weeks post implantation (2-tailed unpaired T-test, error bars show SD). Labelled meshes showed comparable collagen coverage to unlabelled meshes up to 3 months post-implantation, as seen with **E.** Threshold quantification and F representative images of the collagen-stained area ($p > 0.05$ for all time points, 2-tailed unpaired t-test, n≥5 regions of interest) and **F.** representative microscopic images showing Sirius-red stained sections.

Discussion

This report builds on the growing interest in labelling biological polymers for non-invasive imaging (55), adapting an obsolete radio-labelling technique for use with stable iodine and X-ray CT imaging of macromolecular protein-based biomaterials. Previous studies have demonstrated a range of approaches for labelling biomaterials for *in vivo* imaging, including incorporation of radionuclides for nuclear imaging (56, 57), contrast agents for MRI (58-60), as well as high-Z elements for CT imaging (60-62). As it is desirable to have a well-characterised and homogenously labelled product, amino-acid specific attachment has been pursued through a range of bioconjugation and click chemistry approaches – incorporating dyes, nanoparticles, and metal chelates for nuclear imaging and MRI (63-65). However, these reports have typically been restricted to functionalising small soluble proteins, with little having been done previously on pre-formed protein scaffolds. Here there has also been a trend toward developing tyrosine-specific strategies (66-71); being less abundant than the more-established targets of cysteine and lysine, modification of tyrosine provides a route towards more selectively-modified products, with less potential for the disruption of original biological function (68). By modifying tyrosine directly with the imaging agent as demonstrated here however, we sidestep the employment of a bulkier, higher molecular weight carrier molecule for iodine as is necessary when using an functional linker to attain specificity (71, 72). While the labelling approach demonstrate here does lacks the versatility of such bioconjugation approaches (working only with iodine, not other imaging agents of choice), or recent advances in chelate-free labelling (73), it in turn avoids the limitations of poor commercial availability and complex synthesis associated with many bioconjugate or click chemistry reagents.

A recent approach for labelling and imaging collagen with CT involved tethering gold nanoparticles directly to the polymers using the EDC/NHS coupling reaction (61), which provided information on scaffold degradation using *ex vivo*. Lacking the specificity of some of the aforementioned click chemistry approaches, EDC/NHS coupling can target both aspartate and glutamate, as well as the protein c-terminus, which due to their greater abundance in collagen could result in a ~20-fold higher degree of modification than a tyrosine-specific reaction, risking greater alteration of biological function. Secondly the cost of the gold nanoparticles needed for visualisation of larger scale implants would likely preclude its *in vivo* clinical application (61). In contrast, iodination as demonstrated here provides a cheaper and more scalable approach to achieving X-ray visibility, with incorporation of fewer, and lower MW modifications minimising material alteration compared to this, and other nanoparticle-based methods used for MR (59, 60) and CT (60, 61). The use of CT also has the benefit of lower patient radiation dose compared to radionuclide-based approaches to polymer labelling (56), which without the limitations of label half-life also allows imaging at much later times post-transplantation – an important consideration when implants, such as hernia meshes, are often designed to remain *in situ* over months or years. In terms of spatial resolution, CT imaging comparable to MRI in the clinic, and superior to PET or SPECT, as well as typically being cheaper and more widely-available than these alternatives (74).

Despite more recent radio-iodination reactions such as the chloramine-T, Bolton-Hunter, and Iodo-bead-based methods superseding the potassium tri-iodide, and iodine monochloride-based reactions used here (25), the disadvantages that led to the abandonment of these earlier techniques relate specifically to the use of radioactive iodine (^{123}I, ^{124}I ^{131}I). With the main limitation of the KI$_3$ and ICl reactions being incorporation of non-radioactive or carrier iodine alongside, and in competition with the incorporation of radioactive iodine, this becomes a non-issue when using a single, stable isotope. Their slower rate of iodination versus more modern techniques also becomes less problematic when used with stable rather than short half-life isotopes, leaving the use of iodination catalysts such as chloramine-T and iodo-beads again unnecessary. The elimination of

these more expensive catalysts also improves scalability and cost effectiveness of labelling, as macroscopic protein-based implants such as the hernia mesh material used here contain orders of magnitude more material than the solutions of soluble proteins, such as antibodies, for which these radio-iodination reactions were originally designed. However, scope for future work remains in investigating the use of other methods of tyrosine iodination, with an ethanol-based approach having previously provided efficient iodination of complex biological polymers such as wool (75).

With hernia meshes being among the most established biomaterials used in the clinic (~20 million implantations per year globally (35)), the *in vivo* results demonstrated here show promise for translating into improved healthcare outcomes for a considerable population. Complication rates with implanted meshes are commonly over 10%, reaching above 60% where comorbidities such as diabetes, obesity, chronic heart disease, and infection, increase the risk of relapse or complications (76, 77). This can include infection, perforation, tearing, detachment, and migration of the mesh- typically necessitating either their removal, reattachment, or repair. The similarity of biological meshes to native tissue exacerbates the challenge of locating the mesh, making them difficult to delineate from surrounding tissue on the standard CT exam that patients receive, or indeed visually during surgery (33). The ability to non-invasively and longitudinally visualise mesh placement in patients over time should therefore make a useful contribution to diagnosis of complications, and surgical planning.

Currently, the only contrast-enhanced hernia mesh on the market is a synthetic (PVDF - polyvinylidene difluoride) material, loaded with iron-oxide nanoparticles to reduce signal intensity on T_2-weighted MR images (78). Though quite effectively increasing the visibility of implants, including phenomena such as mesh shrinkage (79), the use of MRI on patients with hernia recurrence is less typical than CT (33). One reason for this is the smaller bore size, and lower weight limits of MRI vs CT scanners (80, 81), which becomes a limiting factor given that obesity is one of the main risk factors for initial hernia occurrence, as well as recurrence post-repair. Unfortunately, the bulk-iodination technique demonstrated here works only on protein-based materials, leaving the production of radiopaque synthetic polymer based meshes an area of ongoing research.

However, the compatibility of this labelling technique with other, non-ECM biomaterials such as silk provides ample scope for future implementation of this method. As one of the strongest naturally-occurring materials (82), orders of magnitude above collagen, there is a growing interest in silk for tissue engineering. Though most commonly used a surgical material, a variety of cellular and acellular applications are now emerging, including tendon and ligament grafts, cardiac patches, and vascular constructs (83). Having approximately 6-fold the tyrosine content of collagen, we found a corresponding 6-fold higher radiopacity of silk in the proof-of-concept labelling demonstrated here. Like collagen, silk is difficult to visualise with current medical imaging modalities, with previous methods of incorporating imaging agents including cross-linking (84) and incorporation of platinum coatings (85) – both likely to alter the material properties to a greater degree than iodination of tyrosine.

In summary, we present a fast, cheap, and scalable method to produce X-ray visible protein scaffolds, relying on the iodination of tyrosine. The utility of this approach was demonstrated on a commercially available hernia mesh comprised of decellularised porcine dermis, which showed higher radiopacity up to three months post implantation, compared to unlabelled stock materials. Both labelled and unlabelled materials showed a similar response *in vivo*, indicating the retention of biocompatibility post-labelling. Labelling was also demonstrated on a range of other commercially- available biomaterials, illustrating its potential for tracking protein-based tissue engineering constructs in general. Implanted meshes remained visible *in vivo* at scan times and radiation doses equivalent to and below those used clinically, further demonstrating the translatability of this technique.

Acknowledgements

Methods

Buffer preparation
Glycine 200mM pH 8.6. Tris-HCl 200mM pH 8.6. DPBS (Gibco), HEPES 200mM pH 7.4. insert more details

Animals
Female C57BL/6 mice were purchased from Charles River were 3 weeks old at point of implantation. Mice were housed 5 per individually ventilated cage, at 21°C with normal day/night cycles. All animal studies were licensed under UK Home Office regulations and approved by the UCL Biological Services Ethical Review Committee, with all regulated were in compliance with UCL experimentation guidelines and regulations.

Material labelling
For the triiodide labelling method, 5x10mm hernia mesh samples (Xenmatrix, Bard), or 40x40mm Egg shell membrane were added to either 1mL of HEPES buffer (200 mM, pH 7.4), or PBS (phosphate buffered saline, pH 7.4, GIbco) with 400 µL Lugol's iodine solution (Sigma Aldrich, 32922), and incubated for 24 hours, before being transferred into 0.9% w/v NaCl solution. For the iodine monochloride (McFarlane's) labelling method, mesh samples (5×10mm) were added to either 1 mL of glycine buffer (200 mM, pH 8.6) or Tris-HCl buffer (200 mM, pH 8.6), containing 10 uL of iodine monochloride (Alfa Aesar, 39104), and incubated for 24 hours, before being transferred into 0.9% w/v NaCl solution. Washing was done with 3 changes of fresh saline with 1 hour incubation each on a tube rotator (20 rpm), with a final 24 hour incubation also with rotation. Neuragen nerve guide (Integra Life Sciences) was labelled as above with Lugol's/PBS in 1.5 cm lengths, before washing as above. Silk sutures (Permahand, Ethicon, 3-0 16mm diameter) were de-waxed for 5 minutes in xylene, washed twice with 70% ethanol, and twice with PBS, and labelled with the above Lugol's/PBS method, before washing as above. Purified collagen (Research Grade Jellyfish Collagen, Jellagen), 100 µL at 4mg/mL, was labelled as above with the Lugol's/PBS method, and precipitated with ethanol, before washing as above.

Egg shell Membrane production
David Chau to insert here

Labelling stability
To determine labelling stability in human serum, samples produced using each of the four labelling methods described above (Lugol's/HEPES, Lugol's/PBS, ICl/glycine ICl/Tris) were incubated in 1.5 mL of human serum (Standard Pooled Human Serum, Cambridge Bioscience) at 37°C for 16 days. CT

imaging was perfomed at 0, 1, 2, 5, 7, 9, 12, and 16 days, with region of interest analysis to quantify X-ray absorbance.

Histology

Implanted material was dissected out at 6 weeks post implantation, and freeze-embedded in OCT media (optimal cutting temperature). Samples were cryosectioned (Leica, Bright 5040) at 15 μm and 5 μm onto glass slides (Thermo-Fisher, Superfrost Plus), and left to air dry at room temperature. Tissue was then fixed on the slides in 4% buffered formaldehyde solution for 5 minutes, before washing in phosphate buffered saline (×3). Staining was done using an automated H and E protocol using a Tissue-TEK DRS autostainer (Sakura). Neutrophils and Leukocytes were counted manually at 40× magnification from representative slides at each timepoint using a AE2000 microscope, with five random fields per animal. Digital images were taken at 5 mega-pixel with an eyepiece camera (Dino-Eye-Lite). Collagen staining was done using a Picro Sirius Red kit (Abcam, ab150681) according to the manufacturer's instructions. Representative images of collagen matrixes were taken at 10× magnification, and threshold analysis was done manually using ImageJ's (NIH) measure function to measure % of area coverage (Appendix 2).

SEM and EDS spectroscopy

Collagen scaffold samples were mounted on specimen stubs fitted with adhesive carbon pads, sputter-coated with carbon and examined using a Zeiss Evo50 (Oxford Instruments, Cambridge, UK) scanning electron microscope, with micrographs obtained at an acceleration voltage of 20 kV. Point EDS spectra were acquired using and Oxford Instruments x-act EDS detector running INCA software.

Tensile Strength Testing

Tensile strength of labelled and unlabelled hernia mesh samples (n=5) was evaluated at room temperature using a uniaxial testing device (AGS-X 200kN, Shimadzu), with the following measurement of dimensions prior to testing: 8.298±0.50 mm wide, 14.9±0.24 mm long and 2.16±0.08 mm thick. Each specimen was clamped an average of 3.12±0.44 mm on each end of the long axis before starting the test. During the test the samples were pulled apart at 5mm/min in the Y-axis while recording force and displacement until failure, which was defined as a drop by 50% in the force needed to continue pulling the sample apart. After the initial 'fresh' test, the samples were trimmed at the fracture point and rehydrated in PBS for 20 minutes prior to clamping and retesting under the same conditions (labelled 'Re-test' in the results).

Statistical Analysis

All statistical analysis was performed in Graph Pad Prism 6, according to the details in the main text.

Mesh implantation

Mice were anesthetised with 2% isoflurane in 100% O_2 and surgically implanted with 4×4mm squares of Xenmatrix mesh (BD Bard) subcutaneously under the scruff (n=10 each for labelled and unlabelled mesh).

Zhiping to check and add details?

In vivo imaging

Mice were anesthetised with 2% isoflurane in 100% O_2, and maintained under anaesthesia during imaging with a preclinical micro-CT device (Quantum GX2, PerkinElmer). Mice were scanned at 0,7,14,21,28,35,56, and 84-day timepoints with 4-minute high resolution scans (Voxel size 72 μm, 90 kVp, filters Cu 0.06+Al 0.5). On the 56- and 84-day timepoints mice were also imaged with 18-second (Standard), 8-second (High speed), and 3.9-second (High speed) scans for comparison, also at 90 kVp with Cu 0.06+Al 0.5 filters. 3D ROI analysis was done using Analyze 14.0 software (AnalyzeDirect, Overland Park, KS) using manually-drawn volumes of interest on labelled and unlabelled meshes, and corresponding upper thigh muscles for each animal. Intensity-based semi-automatic segmentation was used to analyse mesh volume over time, which was only possible on the labelled mesh due to its greater radiopacity versus surrounding tissue. Insert details for scans done on the old CT scanner too

References

1. Zhang X, Chen X, Hong H, Hu R, Liu J, Liu C. Decellularized extracellular matrix scaffolds: Recent trends and emerging strategies in tissue engineering. Bioactive Materials. 2022;10:15-31.
2. Stenzel KH, Miyata T, Rubin AL. Collagen as a Biomaterial. Annual review of biophysics and bioengineering. 1974;3(1):231-53.
3. Freedman BR, Mooney DJ. Biomaterials to Mimic and Heal Connective Tissues. Adv Mater. 2019;31(19):e1806695.
4. Sorushanova A, Delgado LM, Wu Z, Shologu N, Kshirsagar A, Raghunath R, et al. The Collagen Suprafamily: From Biosynthesis to Advanced Biomaterial Development. Adv Mater. 2019;31(1):e1801651.
5. Dikmans RE, Negenborn VL, Bouman MB, Winters HA, Twisk JW, Ruhe PQ, et al. Two-stage implant-based breast reconstruction compared with immediate one-stage implant-based breast reconstruction augmented with an acellular dermal matrix: an open-label, phase 4, multicentre, randomised, controlled trial. Lancet Oncol. 2017;18(2):251-8.
6. Reinforcement of Closure of Stoma Site C, West Midlands Research C. Prophylactic biological mesh reinforcement versus standard closure of stoma site (ROCSS): a multicentre, randomised controlled trial. Lancet. 2020;395(10222):417-26.
7. David-Montefiore E, Barranger E, Dubernard G, Detchev R, Nizard V, Darai E. Treatment of genital prolapse by hammock using porcine skin collagen implant (Pelvicol). Urology. 2005;66(6):1314-8.
8. Shoulders MD, Raines RT. Collagen Structure and Stability. Annual review of biochemistry. 2009;78(1):929-58.
9. Di Lullo GA, Sweeney SM, Körkkö J, Ala-Kokko L, San Antonio JD. Mapping the Ligand-binding Sites and Disease-associated Mutations on the Most Abundant Protein in the Human, Type I Collagen. Journal of Biological Chemistry. 2002;277(6):4223-31.
10. Ricard-Blum S. The collagen family. Cold Spring Harb Perspect Biol. 2011;3(1):a004978.
11. Lehmann S, Merk DR, Etz CD, Oberbach A, Uhlemann M, Emrich F, et al. Porcine xenograft for aortic, mitral and double valve replacement: long-term results of 2544 consecutive patients. Eur J Cardio-Thorac. 2016;49(4):1150-6.
12. Ott HC, Clippinger B, Conrad C, Schuetz C, Pomerantseva I, Ikonomou L, et al. Regeneration and orthotopic transplantation of a bioartificial lung. Nature medicine. 2010;16(8):927-33.
13. Kitahara H, Yagi H, Tajima K, Okamoto K, Yoshitake A, Aeba R, et al. Heterotopic transplantation of a decellularized and recellularized whole porcine heart. Interact Cardiov Th. 2016;22(5):571-9.
14. Ott HC, Matthiesen TS, Goh S-K, Black LD, Kren SM, Netoff TI, et al. Perfusion-decellularized matrix: using nature's platform to engineer a bioartificial heart. Nature medicine. 2008;14(2):213-21.
15. Lin K, Zhang D, Macedo MH, Cui W, Sarmento B, Shen G. Advanced Collagen-Based Biomaterials for Regenerative Biomedicine. Advanced functional materials. 2019;29(3).

16.   Gaspar VM, Lavrador P, Borges J, Oliveira MB, Mano JF. Advanced Bottom-Up Engineering of Living Architectures. Adv Mater. 2020;32(6):e1903975.

17.   Walters BD, Stegemann JP. Strategies for directing the structure and function of three-dimensional collagen biomaterials across length scales. Acta biomaterialia. 2014;10(4):1488-501.

18.   Oh HH, Ko YG, Lu H, Kawazoe N, Chen G. Preparation of porous collagen scaffolds with micropatterned structures. Adv Mater. 2012;24(31):4311-6.

19.   Lee A, Hudson AR, Shiwarski DJ, Tashman JW, Hinton TJ, Yerneni S, et al. 3D bioprinting of collagen to rebuild components of the human heart. Science. 2019;365(6452):482-7.

20.   Armstrong JPK, Pchelintseva E, Treumuth S, Campanella C, Meinert C, Klein TJ, et al. Tissue Engineering Cartilage with Deep Zone Cytoarchitecture by High-Resolution Acoustic Cell Patterning. Advanced healthcare materials. 2022;11(24):e2200481.

21.   Liu W, Xu B, Zhao S, Han S, Quan R, Liu W, et al. Spinal cord tissue engineering via covalent interaction between biomaterials and cells. Sci Adv. 2023;9(6):eade8829.

22.   He L, Zhou J, Chen M, Lin CS, Kim SG, Zhou Y, et al. Parenchymal and stromal tissue regeneration of tooth organ by pivotal signals reinstated in decellularized matrix. Nature materials. 2019;18(6):627-37.

23.   Scarfe L, Brillant N, Kumar JD, Ali N, Alrumayh A, Amali M, et al. Preclinical imaging methods for assessing the safety and efficacy of regenerative medicine therapies. NPJ Regenerative medicine. 2017;2(1).

24.   Armstrong JPK, Keane TJ, Roques AC, Patrick PS, Mooney CM, Kuan W-L, et al. A blueprint for translational regenerative medicine. Science translational medicine. 2020;12(572).

25.   Lane DJR, Richardson DR. William Hunter and radioiodination: Revolutions in the labelling of proteins with radionuclides of iodine. The Biochemist. 2011;33(6):34-8.

26.   Neuberger A. Electrometric titration of zein and iodozein. The Biochemical journal. 1934;28(6):1982-92.

27.   Pressman D. The zone of localization of antibodies; the in vivo disposition of anti-mouse-kidney serum and anti-mouse-plasma serum as determined by radioactive tracers. Journal of immunology. 1949;63(4):375-88.

28.   Pressman D, Keighley G. The zone of activity of antibodies as determined by the use of radioactive tracers; the zone of activity of nephritoxic antikidney serum. Journal of immunology. 1948;59(2):141-6.

29.   Pressman D, Eisen HN. The zone of localization of antibodies. V. An attempt to saturate antibody-binding sites in mouse kidney. Journal of immunology. 1950;64(4):273-9.

30.   Tsomides TJ, Eisen HN. Stoichiometric Labeling of Peptides by Iodination on Tyrosyl or Histidyl Residues. Analytical biochemistry. 1993;210(1):129-35.

31.   Robinson JJ. Comparative Biochemical Analysis of Sea Urchin Peristome and Rat Tail Tendon Collagen. Comparative Biochemistry and Physiology Part B: Biochemistry and Molecular Biology. 1997;117(2):307-13.

32.   Gross J, Dumsha B, Glazer N. Comparative biochemistry of collagen some amino acids and carbohydrates. Biochimica et biophysica acta. 1958;30(2):293-7.

33.   Gavlin A, Kierans AS, Chen J, Song C, Guniganti P, Mazzariol FS. Imaging and Treatment of Complications of Abdominal and Pelvic Mesh Repair. Radiographics. 2020;40(2):432-53.

34.   Rakic S, LeBlanc KA. The Radiologic Appearance of Prosthetic Materials Used in Hernia Repair and a Recommended Classification. Am J Roentgenol. 2013;201(6):1180-3.

35.   Baylón K, Rodríguez-Camarillo P, Elías-Zúñiga A, Díaz-Elizondo J, Gilkerson R, Lozano K. Past, Present and Future of Surgical Meshes: A Review. Membranes. 2017;7(3).

36.   Mc FA. Efficient trace-labelling of proteins with iodine. Nature. 1958;182(4627):53.

37.   Li CH. Kinetics and Mechanism of 2,6-Di-iodotyrosine Formation1. Journal of the American Chemical Society. 1942;64(5):1147-52.

38.   Jeong Y, Jin M, Kim KS, Na K. Biocompatible carbonized iodine-doped dots for contrast-enhanced CT imaging. Biomaterials Research. 2022;26(1).

39.   Zhang Y, Iwata T, Nam K, Kimura T, Wu P, Nakamura N, et al. Water absorption by decellularized dermis. Heliyon. 2018;4(4).

40.   Cowgill RW. Fluorescence and the structure of proteins IV. Iodinated tyrosyl residues. Biochimica et Biophysica Acta (BBA) - Biophysics including Photosynthesis. 1965;94(1):74-80.

41.   MacPherson DS, McPhee SA, Zeglis BM, Ulijn RV. The Impact of Tyrosine Iodination on the Aggregation and Cleavage Kinetics of MMP-9-Responsive Peptide Sequences. ACS Biomaterials Science & Engineering. 2022;8(2):579-87.

42.   Bensusan HB, Scanu A. Fiber Formation from Solutions of Collagen. II. The Role of Tyrosyl Residues. Journal of the American Chemical Society. 1960;82(18):4990-5.

43.   Wolff J, Covelli I. Factors in the Iodination of Histidine in Proteins. European Journal of Biochemistry. 1969;9(3):371-7.

44.   Farole A, Jamal BT. A bioabsorbable collagen nerve cuff (NeuraGen) for repair of lingual and inferior alveolar nerve injuries: a case series. Journal of oral and maxillofacial surgery : official journal of the American Association of Oral and Maxillofacial Surgeons. 2008;66(10):2058-62.

45.   Bedar M, van Wijnen AJ, Shin AY. Safety of Allogeneic Mesenchymal Stem Cell Seeding of NeuraGen Nerve Guides in a Rabbit Model. Tissue engineering Part C, Methods. 2023;29(2):43-53.

46.   Liodaki E, Bos I, Lohmeyer JA, Senyaman O, Mauss KL, Siemers F, et al. Removal of collagen nerve conduits (NeuraGen) after unsuccessful implantation: focus on histological findings. J Reconstr Microsurg. 2013;29(8):517-22.

47.   Han C, Chen Y, Shi L, Chen H, Li L, Ning Z, et al. Advances in eggshell membrane separation and solubilization technologies. Front Vet Sci. 2023;10:1116126.

48.   Park S, Gwon Y, Kim W, Kim J. Rebirth of the Eggshell Membrane as a Bioactive Nanoscaffold for Tissue Engineering. ACS Biomater Sci Eng. 2021;7(6):2219-24.

49.   Sun P, Yan S, Zhang L, Zhang C, Wu H, Wei S, et al. Egg Shell Membrane as an Alternative Vascular Patch for Arterial Angioplasty. Frontiers in bioengineering and biotechnology. 2022;10.

50.   Aggarwal A, Sah MK. Eggshell membrane in skin tissue engineering and wound healing. Natural Polymers in Wound Healing and Repair2022. p. 417-35.

51.   D'Ambra I, Merquiol L. Jellyfish from Fisheries By-Catches as a Sustainable Source of High-Value Compounds with Biotechnological Applications. Marine drugs. 2022;20(4).

52.   Ahmed Z, Powell LC, Matin N, Mearns-Spragg A, Thornton CA, Khan IM, et al. Jellyfish Collagen: A Biocompatible Collagen Source for 3D Scaffold Fabrication and Enhanced Chondrogenicity. Marine drugs. 2021;19(8).

53.   Deeken CR, Eliason BJ, Pichert MD, Grant SA, Frisella MM, Matthews BD. Differentiation of Biologic Scaffold Materials Through Physicomechanical, Thermal, and Enzymatic Degradation Techniques. Annals of surgery. 2012;255(3):595-604.

54.   Atli E, Uyanik SA, Oguslu U, Cevik Cenkeri H, Yilmaz B, Gumus B. Radiation doses from head, neck, chest and abdominal CT examinations: an institutional dose report. Diagn Interv Radiol. 2021;27(1):147-51.

55.   Li R, Ng TSC, Garlin MA, Weissleder R, Miller MA. Understanding the In Vivo Fate of Advanced Materials by Imaging. Advanced functional materials. 2020.

56.   Patrick PS, Bear JC, Fitzke HE, Zaw-Thin M, Parkin IP, Lythgoe MF, et al. Radio-metal cross-linking of alginate hydrogels for non-invasive in vivo imaging. Biomaterials. 2020;243.

57.   Pang F, Li Y, Zhang W, Xia C, He Q, Li Z, et al. Biodegradable 131-Iodine-Labeled Microspheres: Potential Transarterial Radioembolization Biomaterial for Primary Hepatocellular Carcinoma Treatment. Advanced healthcare materials. 2020;9(13).

58.   Karfeld-Sulzer LS, Waters EA, Kohlmeir EK, Kissler H, Zhang X, Kaufman DB, et al. Protein polymer MRI contrast agents: Longitudinal analysis of biomaterials in vivo. Magn Reson Med. 2011;65(1):220-8.

59.   Mahmoudi M, Zhao M, Matsuura Y, Laurent S, Yang PC, Bernstein D, et al. Infection-resistant MRI-visible scaffolds for tissue engineering applications. BioImpacts. 2016;6(2):111-5.

60.   Barnett BP, Arepally A, Stuber M, Arifin DR, Kraitchman DL, Bulte JWM. Synthesis of magnetic resonance–, X-ray– and ultrasound-visible alginate microcapsules for immunoisolation and noninvasive imaging of cellular therapeutics. Nat Protoc. 2011;6(8):1142-51.

61.   Finamore TA, Curtis TE, Tedesco JV, Grandfield K, Roeder RK. Nondestructive, longitudinal measurement of collagen scaffold degradation using computed tomography and gold nanoparticles. Nanoscale. 2019;11(10):4345-54.

62.   Arifin DR, Manek S, Call E, Arepally A, Bulte JWM. Microcapsules with intrinsic barium radiopacity for immunoprotection and X-ray/CT imaging of pancreatic islet cells. Biomaterials. 2012;33(18):4681-9.

63.   Kenry, Liu B. Bio-orthogonal Click Chemistry for In Vivo Bioimaging. Trends in Chemistry. 2019;1(8):763-78.

64.   Meyer J-P, Adumeau P, Lewis JS, Zeglis BM. Click Chemistry and Radiochemistry: The First 10 Years. Bioconjugate chemistry. 2016;27(12):2791-807.

65.   Bauer D, Sarrett SM, Lewis JS, Zeglis BM. Click chemistry: a transformative technology in nuclear medicine. Nat Protoc. 2023.

66.   Gavrilyuk J, Ban H, Nagano M, Hakamata W, Barbas CF. Formylbenzene Diazonium Hexafluorophosphate Reagent for Tyrosine-Selective Modification of Proteins and the Introduction of a Bioorthogonal Aldehyde. Bioconjugate chemistry. 2012;23(12):2321-8.

67.   Ban H, Nagano M, Gavrilyuk J, Hakamata W, Inokuma T, Barbas CF, 3rd. Facile and stabile linkages through tyrosine: bioconjugation strategies with the tyrosine-click reaction. Bioconjugate chemistry. 2013;24(4):520-32.

68.   Spicer CD, Davis BG. Selective chemical protein modification. Nature communications. 2014;5(1).

69.   Allan C, Kosar M, Burr CV, Mackay CL, Duncan RR, Hulme AN. A Catch-and-Release Approach to Selective Modification of Accessible Tyrosine Residues. Chembiochem. 2018;19(23):2443-7.

70.   Li BX, Kim DK, Bloom S, Huang RYC, Qiao JX, Ewing WR, et al. Site-selective tyrosine bioconjugation via photoredox catalysis for native-to-bioorthogonal protein transformation. Nature chemistry. 2021;13(9):902-8.

71.   Declas N, Maynard JRJ, Menin L, Gasilova N, Götze S, Sprague JL, et al. Tyrosine bioconjugation with hypervalent iodine. Chem Sci. 2022;13(43):12808-17.

72.   Dong S, Moroder L, Budisa N. Protein Iodination by Click Chemistry. Chembiochem. 2009;10(7):1149-51.

73.   Patrick PS, Bogart LK, Macdonald TJ, Southern P, Powell MJ, Zaw-Thin M, et al. Surface radio-mineralisation mediates chelate-free radiolabelling of iron oxide nanoparticles. Chem Sci. 2019;10(9):2592-7.

74.   James ML, Gambhir SS. A Molecular Imaging Primer: Modalities, Imaging Agents, and Applications. Physiological reviews. 2012;92(2):897-965.

75.   Richards HR, Speakman JB. The Iodination of Wool. Journal of the Society of Dyers and Colourists. 1955;71(9):537-44.

76.   Harris HW, Primus F, Young C, Carter JT, Lin M, Mukhtar RA, et al. Preventing Recurrence in Clean and Contaminated Hernias Using Biologic Versus Synthetic Mesh in Ventral Hernia Repair. Annals of surgery. 2021;273(4):648-55.

77.   Dai W, Chen Z, Zuo J, Tan J, Tan M, Yuan Y. Risk factors of postoperative complications after emergency repair of incarcerated groin hernia for adult patients: a retrospective cohort study. Hernia. 2018;23(2):267-76.

78.   Lechner M, Meissnitzer M, Borhanian K, Bittner R, Kaufmann R, Mayer F, et al. Surgical and radiological behavior of MRI-depictable mesh implants after TAPP repair: the IRONMAN study. Hernia. 2019;23(6):1133-40.

79.   Kuehnert N, Kraemer NA, Otto J, Donker HCW, Slabu I, Baumann M, et al. In vivo MRI visualization of mesh shrinkage using surgical implants loaded with superparamagnetic iron oxides. Surgical Endoscopy. 2011;26(5):1468-75.

80.	Uppot RN. Technical challenges of imaging & image-guided interventions in obese patients. The British journal of radiology. 2018.

81.	Uppot RN, Sahani DV, Hahn PF, Gervais D, Mueller PR. Impact of Obesity on Medical Imaging and Image-Guided Intervention. Am J Roentgenol. 2007;188(2):433-40.

82.	Vepari C, Kaplan DL. Silk as a biomaterial. Prog Polym Sci. 2007;32(8-9):991-1007.

83.	Bandyopadhyay A, Chowdhury SK, Dey S, Moses JC, Mandal BB. Silk: A Promising Biomaterial Opening New Vistas Towards Affordable Healthcare Solutions. Journal of the Indian Institute of Science. 2019;99(3):445-87.

84.	Francis NK, Pawar HS, Ghosh P, Dhara S. In Situ Iodination Cross-Linking of Silk for Radio-Opaque Antimicrobial Surgical Sutures. ACS Biomaterials Science & Engineering. 2016;2(2):188-96.

85.	Guglielmi G, Benati A, Perini S. Endovascular Embolization with Radiopaque Silk Threads: A Feasibility Study in Swine. Interventional Neuroradiology. 2016;12(2):109-12.